IET Radar, Sonar & Navigation

WILEY The Institution of Engineering and Technology

ORIGINAL RESEARCH

4D radar simulator for human activity recognition

Junyu Zhou | **Julien Le Kernec** ⓘ

James Watt School of Engineering, University of Glasgow, Glasgow, UK

Correspondence

Julien Le Kernec, James Watt School of Engineering, University of Glasgow, James Watt South Building, University Avenue, Glasgow G12 8QQ, UK.
Email: julien.lekernec@glasgow.ac.uk

Abstract

Millimetre-wave radar has been widely used in health monitoring and human activity recognition owing to its improved range resolution and operation in a variety of environmental conditions. With the MIMO antenna array, 4D radar is increasingly employed in autonomous driving, while its application in assisted living is recent and therefore the value added compared to the increase in signal processing and hardware requirements is still an open question. A model for 4D Time-division multiplexing (TDM) multiple-input-multiple-output (MIMO) frequency-modulated Continuous wave radar is established using the human activities from the HDM05 motion capture dataset. The simulator produces an end-to-end simulation, including four human motions (jumping Jack, kick, punch, and walk), signal time of flight, noise, MIMO signal processing, and classification. Different pre-processing and point cloud-based methods are compared to obtain an average classification accuracy of 90% with PointNet. This study simulates a specific 4D TDM MIMO radar configuration to benchmark signal pre-processing algorithms, which can also assist other researchers to generate range-Doppler-time (range-Doppler time) point cloud data sets for human activities testing different radar configurations, array configurations, and activities saving valuable time in human resources and hardware development before prototyping to assess expected performances.

KEYWORDS

radar, signal processing

1 | INTRODUCTION

Due to the ageing of population, monitoring the health condition of elderly people becomes a significant problem. Among popular products on the market, wearable devices are one type of competing health-monitoring technologies, but their intrusiveness, fragility, and battery-operated necessity limit the application range sometimes. Wearable devices also have a weakness with compliance as they must be worn to be effective. This may not be the case when people live with cognitive decline forgetting to wear them or people simply do not want to wear them. In competition with wearable technology, electromagnetic waves have emerged as one of the most effective indoor monitoring modalities due to the appealing qualities of radar, including its non-obstructive illumination, non-intrusive sensing, insensitivity to lighting conditions, and privacy preservation [1].

In the field of human activity recognition (HAR), 4D MIMO frequency-modulated Continuous wave (FMCW) radar is an ideal choice, which has no blind ranges compared with pulse radar. 4D refers to the range, velocity, azimuth, and elevation, which provide complete information about the target velocity and location in 3D space [2]. While many researchers have been working on classification models related to deep learning, more work is expected to focus on signal pre-processing for enhanced classification accuracy especially for 4D radar since it can vary in geometry, hardware, and signal processing techniques.

A mainstream method to achieve activity recognition is to use micro-Doppler (mD) signatures. The authors in ref. [3] explained the mD signature comprehensively and illustrated the phenomenon by explaining the kinematic features seen in the signature with the motion of humans, quadrupeds and birds observed by the radar. The focus was on modelling a

simplified CW radar phase delay model with a vector partitioning the line of sight range in bins. To simulate the mD phenomenon in [3], a vector is defined representing the distance divided into range bins. Range bins reflect the range resolution of the radar, which is defined by the bandwidth of the signal. A radar system would need to process the received signal with stretch processing for an FMCW radar or pulse compression for a signal that was fully digitised to obtain the range information of the target. The author in ref. [3] calculates the amplitude of the reflection based on canonical geometric shapes, such as ellipsoids and spheres, and based on the distance from the radar to the target determines which range bin in the distance vector this target would fall into. Then the phase delay would be calculated based on the time of flight. A Dirac is then added at that range bin with the polar form with the calculated amplitude and phase. This is a 'shortcut' to reduce the computational load as opposed to simulating the full wave, but this means that the raw data and the range information cannot be exploited as they are not representative of the radar operation. It was shown in [4] that the algorithm modelling full waves was more computationally intensive than the algorithm in [3]. However, it gave more details in simulated mD signatures, especially in acceleration and deceleration phases [4]. In [5], the authors also used mD signatures and benchmarked the classification performance as a function of aspect angle by comparing eight radar systems. The authors in [5] have proven that the monostatic radar system recognises activities best when the aspect angle of targets is less than 30°, whereas multistatic and interferometric radar geometries can recognise activities consistently across the range variations. Hence, we choose the centralised MIMO radar for simulation. Shelly designed an open-source simulation tool for creating micro-Doppler data in passive WiFi radar scenarios [6], and simulated data with a full wave simulator indicated 8% improvement over using real mD signatures.

In [7], the authors proposed a hierarchical activity classification approach and combined 13 features extracted from Doppler spectra, including energy features, physical features, image-based features, cadence velocity diagram and singular value decomposition features, yielding 95.4% accuracy to classify six activities. However, one common problem of utilising mD signatures is that features should be carefully handpicked based on the dataset, which limits the universality of the algorithm. Furthermore, with the 2D antenna array, micro-Doppler simulations can be extrapolated to 4D radar. Adding the other data representation from the perspective of the range domain allows us to extract point clouds, which provide more exact information about detected targets. Based on the range-Doppler surface (RDS) method, a range migration compensation method based on Keystone transformation for high-quality imaging was proposed [8]. In addition, an adaptive threshold for 2D Constant False Alarm Rate (CFAR) detection was applied to locate the extended targets in the Range Doppler Map (RDM). In [9], the authors selected eight activities from the Carnegie Mellon University mocap dataset and generated point clouds by extracting the isosurface from the radar-Doppler-time (range-Doppler time (RDT)) matrix.

In the paper, body parts could be separated by intensity, and the contour of RDM was retained for surface extraction. Although this method simplifies the complexity of computation, it may result in the loss of RDM information. Instead of separating body parts, our algorithm retains the whole RDM filtered by 2D CFAR to avoid information losses.

One traditional method of dealing with point clouds is to match the cloud points with human bones. The authors in ref. [10] utilised millimetre wave radar to identify the primary motions of the human body and to detect and monitor 15 separate bone joints through radar reflection signals. The normalised value of the distance, angle, and power level of the reflected signal at each location was assigned to the RGB channel using a radar-to-image representation. Finally, a split CNN architecture was used to predict where the accurate skeleton joints would be in three dimensions, and ultimately, to recognise human motions. However, this method is unreliable as it frequently fails to capture some bone reflections. PointNet proposed in 2016 [11] is a deep learning architecture for processing point cloud data directly. The main idea is to use shared multi-layer perceptions to extract the global feature and output k scores, where k is the number of categories. This network greatly retains the characteristics of point clouds, including the rotation in-variance and permutation in-variance by applying T-net and max-pooling, respectively. Besides the method of dealing with point clouds directly, some other well-known representations of point cloud data include voxelisation and tabularisation. However, these two methods have some disadvantages. After the point clouds are voxelised, congested voxels may result in the loss of information, and empty voxels will increase the amount of unnecessary computation [12]. Tabularisation saved more storage space and allowed more features than voxelisation, but the sorting and padding processing are complicated when the number of point clouds is huge [13]. Therefore, PointNet is applied in the paper and the average classification accuracy of four human activities reaches 90%.

To summarise, the main contributions are as follows:

1. Propose a 4D Time-division multiplexing (TDM) radar simulator that can simulate radar returns with 12Tx-16Rx radar configuration that generates all the radar data representation domains, including raw data, range-time, spectrogram, range-Doppler, and range-angle with MIMO CFAR detection.
2. Propose Range-Doppler-Time representations based on the proposed 4D TDM MIMO radar simulator extracting regions of interest automatically with 2D MIMO CFAR for activity recognition, including jumping Jack, kick, punch, and walk with a specific sampling for input into PointNet achieving 90% classification accuracy, which verifies the correctness of our radar model.

The paper is organised as follows: In Section 2, the 4D TDM FMCW radar working principle is briefly introduced. In Section 3, the methodology is presented for the implementation of the 4D radar model and human activity classification.

In Section 4, the results are presented and discussed. Finally, in Section 5, conclusions and ideas for further work are provided.

2 | TDM MIMO FMCW RADAR WORKING PRINCIPLE

The basic working principle of MIMO radar involves the transmission of signals at different transmit antenna locations and the reception of multiple reflections from targets using multiple receiving antennas, which improves detection performance through the MIMO gain and allows to resolve targets in angle. This angular resolution depends on the number of elements and the geometrical arrangement of the transmit and receive antennas. Multiplexing strategies and antenna array configuration are crucial parts of the MIMO radar system explained in this section [2, 14].

Different signals can be transmitted for MIMO radar implementation, such as OFDM for integrated sensing and communication [15], Orthogonal Time Frequency Space Modulation (OTFS) [16], and chirp, which is widespread in automotive applications for ADAS. For the remainder of the paper, we will concentrate on the chirp signal for the MIMO considerations. Other waveforms are out of the scope of this research work.

- **Multiplexing strategies:** MIMO radar systems use multiplexing methods to transmit and receive signals from multiple antennas to achieve improved spatial resolution, target detection, and interference mitigation performance. Some common multiplexing strategies include TDM, frequency-division multiplexing (FDM), Doppler-division multiplexing and code-division multiplexing (CDM).
- In TDM, the multiple transmitting (Tx) antennas in a MIMO radar system transmit signals one at a time in a sequential manner. Each transmit antenna for an FMCW radar system is responsible for periodically transmitting signals sequentially [17]. All receiving (Rx) antennas are receiving the back-scattered signals at the receiver. The full radar data cube is complete once all the transmit antennas have sent their chirp pulse, and then the cycle repeats. In FDM, transmitted signals are separated in frequency, and the receiver processes the signals based on their respective frequency bands. Frequency-division multiplexing allows simultaneous transmission/reception from multiple antennas at different frequency bands, but it may require wider bandwidth than other multiplexing methods or a reduced bandwidth for each chirp to allow for the separation of the transmit pulses so they do not interfere with each other. This may reduce the range resolution in the latter case. Doppler-division multiplexing is to introduce frequency bias in the Doppler dimension to separate the channels [18]. In this case, the range resolution is not sacrificed; however, the range of Doppler speeds is divided by the number of simultaneous transmit compared to a single pulse. About CDM, the signals are separated at the receiver based on the unique codes used by each antenna, which causes

interference in the Doppler dimension, making it easy to overwhelm small targets. As HAR requires a large dynamic range of echo energy, CDM is not appropriate in simulation. By contrast, TDM is a simple and low-cost scheme in practical implementation, and the maximum detectable speed satisfies the requirement of the situation. Therefore, it is adopted as our MIMO scheme for 4D radar.

- **Antenna array configuration:** The antenna array in an MIMO radar system is a crucial component that enables the transmission and reception of signals from multiple antennas to achieve improved angular resolution [14, 19]. The array configuration refers to the number of elements, type, and placement. The monostatic MIMO radar is considered in our research, and thus, the distance between transmitters and receivers is negligible. For instance, Figure 1 shows a radar system with 2Tx and 4Rx antennas, and the wave path difference between two adjacent Rx antennas can be estimated by $d\,sin\theta$, and the phase difference is $\Delta\phi = \frac{2\pi d\,\sin(\theta)}{\lambda}$, where d is the distance between two adjacent Rx antennas. For physical antenna configuration, the conception of the virtual array can be introduced to help analyse signals for each channel, aiming to produce the same target response as the original physical configuration. Figure 1 shows the physical antenna configuration of a 2Tx-4Rx system and its equivalent virtual array.

The same principle applies to two-dimensional arrays. As the angular separation relies on the phase difference of signals received by Rx antennas, adding antennas in elevation enables the radar system to obtain elevation angle information. This constitutes the four-dimensional radar with range, Doppler, azimuth, and elevation that will return the exact coordinates of the target in a solid angle at a given range from the radar, travelling at a given speed.

3 | METHODOLOGY

We achieve the goal by building three models: the human activity model, the 4D MIMO radar model, and the classification model. Figure 2 gives a synoptic of the methodology detailed in this section. The code for this simulator can be found on github[1].

3.1 | Human activity model

The HDM05 database [20] contains the mocap file for different activities recording 31 joints, which can be mapped to a 24-joint skeletal kinematic chain [21]. It was further simplified to a 21-joint model owing to three joints (neck, left clavicle, and right clavicle) were not separated in HDM05. Ellipsoids are used to emulate the radar cross-section of the different body parts in the human model that will constitute

---

[1] https://github.com/JASONZ777/4D-radar-simulator.git

the reflective surfaces for the construction of the simulated radar signatures of human activities, which form an ellipsoid model in Figure 2. The 4 activities chosen for the simulation are jumping, Jack, kick, punch, and walk, since these are the activities that have the most samples in the HDM05 database.
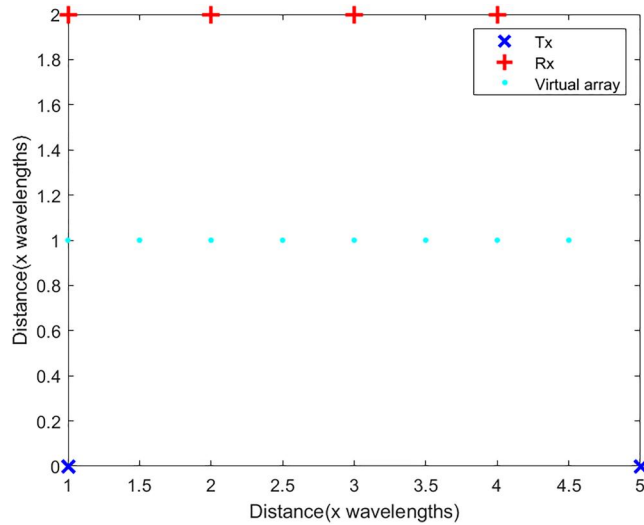

FIGURE 1 A 2Tx-4Rx antenna array and its virtual channels.

3.2 | 4D MIMO radar model

3.2.1 | Simulation parameters

In this section, the simulation parameters are presented and some radar theoretical performance metrics are calculated to contextualise the 4D radar capabilities. The radar parameters in Table 1 have been chosen for simulation.

The choice of frequency was highly dependent on the computational load going higher in frequencies:

- At 12 GHz, the simulator takes 1.5 h with a 12th Gen Intel (R) i9-12900H and 32 GB of RAM to complete the generation of chirps, interaction with the motion capture data and the whole signal processing as described in Figure 2 to generate 1 sample for the machine learning algorithm. This corresponds to 1 whole motion capture file lasting approximately 3s.
- At 77 GHz, the simulator runs out of memory and cannot generate samples.

We have provided the code at https://github.com/JASONZ777/4D-radar-simulator.git for researchers in possession of more powerful machines to simulate higher frequencies to model more recent platforms at 60 and 77 GHz. Furthermore, the reason is also due to the maximum detectable
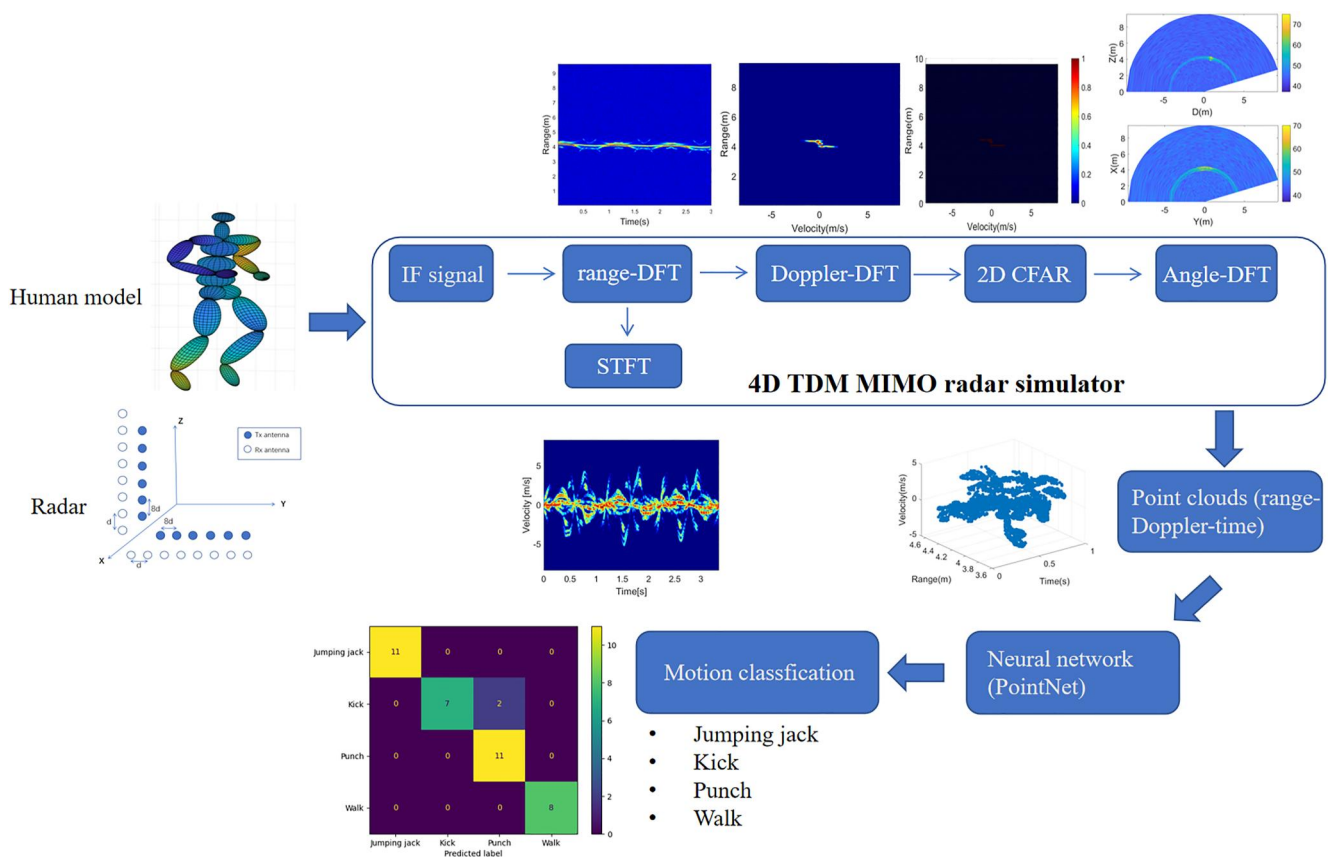

FIGURE 2 Synoptic of the methodology – human modelling from motion capture data, 4D Time-division multiplexing MIMO radar simulation and classification models using point clouds as input.

velocity without ambiguity as we are getting 8.33 m/s at 12 GHz with 12 transmitters as this is a TDM radar. This means that the pulses are transmitted sequentially through every channel. We would only get a maximum detectable velocity of 1.66 m/s and 1.3 m/s at 60 and 77 GHz, respectively. This would result in Doppler aliasing in the micro-Doppler signatures.

As described, the radar is placed at a relative position of $(-4,1,1)$ m with respect to the origin of the referential $(0,0,0)$ around which the activities are performed. The target is therefore 3–5 m away from the radar. The sweep time of each chirp t_c dictates the unaliased maximum detectable velocity. In our application, walking would generate the maximum Doppler spread. Considering that walking can range from 0.2 m/s to 2 m/s for a very slow person with an affected gait to a very fast

walker. Considering walking, the walking speed corresponds to the torso. However, a leg swing can reach more than 3 times that speed during the gait cycle. Most velocity components induced by human activities in the context of assisted living should be below 8 m/s. Therefore, we selected $t_c = 62.5$ µs giving a maximum detectable velocity at 8.33 m/s, therefore avoiding aliasing in the mD signatures. This is given by Equation (3). Since the original frame rate of mocap data is only 120 Hz and is not sufficient for radar operation, given the Nyquist sampling theorem, interpolation is required to satisfy our determined sampling rate $F_s = N_s/t_c = 4.096$ MHz. The number of total chirps for one radar frame is $N_{tc} = t_f/t_c = 1600$ at the receiver. Given that the shape of the skeleton model should be fixed during the interpolation process, a piece-wise cubic Hermit interpolation is applied, which guarantees no distortion of the human model. The placement of transmitting and receiving antennas is described in Figure 3, which creates 192 virtual channels. However, some virtual arrays overlap and we just consider virtual channels created by antenna pairs along the y and z axes. They determine the angle resolution in azimuth and elevation, respectively. The number of virtual channels per axis is $T_yR_y = T_zR_z = 48$.

From these parameters, the detection limits and resolution of range, velocity and angle are estimated to meet the performance of the simulated system.

Range detection is achieved by performing an FFT in the fast-time dimension. The maximum detectable range limit and minimum distinguishable distance are provided in Equations (1) and (2).
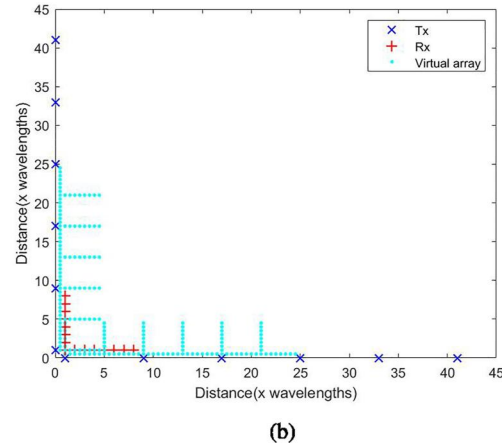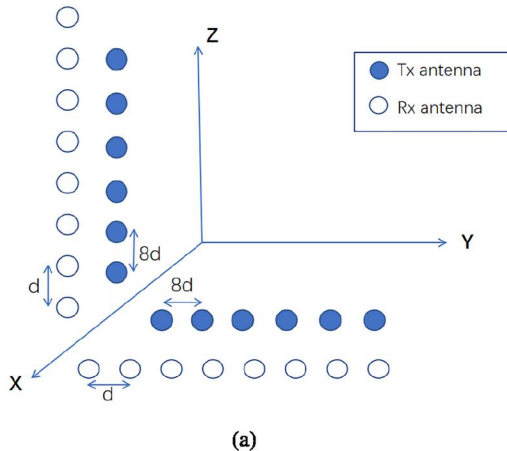
TABLE 1 Radar parameters for simulation.

Parameter	Description	Value
f_c	Radar starting frequency	12 GHz
Λ	Radar wavelength	25 mm
t_f	Time duration per radar frame	100 ms
(x_R, y_R, z_R)	Radar position	(-4,1,1) m
t_c	Sweep time per chirp	62.5 µs
N_s	Number of samples per chirp	256
B_w	Radar bandwidth	4 GHz
S	The sampling slope of one chirp	6.4×10^{13} Hz/s
C	The speed of light	3×10^8 m/s
T_y	Number of Tx along y axis	6
T_z	Number of Tx along z axis	6
R_y	Number of Rx along y axis	8
R_z	Number of Tx along z axis	8
d_R	Distance between adjacent Rx antennas	$\lambda/2$
d_T	Distance between adjacent Tx antennas	4λ

$$r_{max} = \frac{cF_s}{2s} = 9.6 \ m \tag{1}$$

$$r_{dis} = \frac{c}{2B_w} = 3.75 \ cm \tag{2}$$

when the radar system works in the TDM mode and transmitters take turns transmitting radar signals during different chirp slots. Therefore, the number of actual working chirps for

FIGURE 3 12Tx-16Rx MIMO 3D antenna array. (a) MIMO array for 4D radar – 12Tx-16Rx element positions. (b) 12Tx-16Rx element and virtual channels positions.

every Tx antenna is around $N_c = N_{tc}/(T_y + T_z) \simeq 133$ for the 12-Tx radar system. Doppler is derived by looking at the speed of phase variations across range bins in slow time. An FT is performed in the slow time direction for each range bin over 0.1s to form a range-Doppler map. The maximum detectable velocity and minimum unambiguous velocity are obtained by Equations (3) and (4), respectively.

$$|v_{\max}| = \frac{\lambda}{4(T_y + T_z)t_c} = 8.33 \ m/s \qquad (3)$$

$$v_{dis} = \frac{\lambda}{2N_c t_c (T_y + T_z)} = \frac{\lambda}{2t_f} = 0.125 \ m/s \qquad (4)$$

The angles azimuth (α) and elevation(β) are derived by exploiting the phase differences between the received signals at different array elements. Similar to the previous discussion about 2Tx-4Rx radar, the maximum angle of arrival (AoA) is limited by: $\Delta\phi < \pi$, so the range of AoA could be derived:

$$-\sin^{-1}\left(\frac{\lambda}{2d_r}\right) \leq \alpha, \beta < \sin^{-1}\left(\frac{\lambda}{2d_r}\right) \qquad (5)$$

when d_r is equal to $\lambda/2$, the detectable angles range from $-90°$ to $90°$. About the angular resolution, the phase difference induced from different AoA ($\Delta\Phi$) is considered. According to Fourier transform, to distinguish two AoA, $\Delta\Phi > \frac{2\pi}{R_y \cdot T_y}$ should be satisfied. Therefore, angular resolution is then in Equation (6), where θ refers to the estimated AoA.

$$\alpha, \beta_{res} = 2sin^{-1}\left(\frac{\lambda}{2(R_y \cdot T_y)d_r cos(\theta)}\right) \qquad (6)$$

From Equation (6), it is clear that as the AoA increases, the angular resolution decreases gradually and non-linearly. When the estimated angle is about $0°$, the detection resolution reaches the maximum $2/(R_y \cdot T_y)$. In the simulation, there are 48 virtual channels for each axis, so the minimum distinguishable angle is $2.38°$. The azimuth and elevation with respect to the radar are close to $0°$, which indicate that more body parts could be detected and distinguished.

The radar performances are summarised in Table 2.

3.2.2 | Waveform generation

Our method to simulate signals differs from Chen's approach. Instead of just using the amplitude and signal delay based on a CW model, our model keeps the whole transmitted signal and echoes to simulate a real FMCW radar system. For 1Tx-1Rx, the transmitted sinusoidal waveform can be represented as $x(t) = \cos(2\pi f_c t + \pi s t^2)$. Here, f_c is the starting frequency, and s is the slope of the radar chirp. In the simulation, the complex signal is used, so the transmitted signal turns to:

$$x_T(t) = e^{j\left(2\pi f_c t + \pi s t^2\right)} \qquad (7)$$

For a motionless object at a distance of r from the radar, the transmitted signal will be reflected after it reaches the target. The time duration in the air is $\tau = 2r/c$, and the received signal is:

$$x_R(t) = \sqrt{\sigma}e^{j\left(2\pi f_c(t-\tau) + \pi s(t-\tau)^2\right)} \qquad (8)$$

where in Equation (8), σ is the radar cross section (RCS), which measures the strength of an object's reflectivity and is a function of the object's orientation and the radar-transmitted frequency. The authors in ref. [22] provide an approximation of the ellipsoid back-scattering model, which is applied in our simulation to calculate RCS. The received signal is then mixed with the transmitting ones and goes through a low-pass filter to generate an intermediate frequency (IF) signal:

$$x_{IF}(t) = x_T(t) \cdot \overline{x_R(t)} \approx \sqrt{\sigma}e^{j2\pi(s\tau t + f_c\tau)} \qquad (9)$$

Since our human skeleton model is established using 20 body segments, the final IF signal for simulation is the coherent superposition of the IF signal generated from each body segment.

For the MIMO radar system, phase differences among channels occur because the antenna locations for the transmitters and receivers vary increasing spatial diversity, which allows the radar system to obtain the angle information. When 4D radar operates in the TDM mode, transmitting antennas work in turn. All Rx antennas receive signals with phase differences, which can be analysed independently for antennas along Y and Z axes as shown in Figure 3. We suppose t_y, t_z indicate the Tx antenna index ranged from 0 to 5, and r_y, r_z refer to the Rx antenna index ranging from 0 to 7. Then, for each Tx-Rx antenna pair, signals in one chirp are calculated as follows:

$$x_{t_y,r_y}(t) = \sqrt{\sigma}e^{j\left(2\pi\left(f_c(t-\tau) + \pi s(t-\tau)^2\right) + \frac{f_c}{c}(8t_y + r_y)d_R sin(\alpha)\right)} \qquad (10)$$

$$x_{t_z,r_z}(t) = \sqrt{\sigma}e^{j\left(2\pi\left(f_c(t-\tau) + \pi s(t-\tau)^2\right) + \frac{f_c}{c}(8t_z + r_z)d_R sin(\beta)\right)} \qquad (11)$$

T A B L E 2 Detection performance parameters.

Parameter	Description	Value
$r_{\max}$	Maximum detectable range	9.6 m
r_{dis}	Minimum distinguishable distance	3.75 cm
$|v_{\max}|$	Maximum detectable velocity	8.33 m/s
v_{dis}	Minimum unambiguous velocity	0.125 m/s
A_{range}	Detectable angle range	$\pm90°$
A_{dis}	Minimum distinguishable angle	$2.38°$

In Equations (12) and (13), α and β refer to azimuth and elevation, respectively. Accordingly, IF signals should also be revised to $x_{IF}(t) = x_{t_{y(z)}}(t) \cdot x_{t_{y(z)}, \bar{r}_{y(z)}}(t)$. In addition, to evaluate the model's robustness to noise, free space losses are neglected and white Gaussian noise is added. Typically, the minimum signal-to-noise ratio (SNR) in indoor applications should range from 15 to 20 dB. Therefore, we test echoes with an SNR equal to 20 dB and present the final mixed IF signal in Equation (12), where $Z(t)$ follows Gaussian distribution.

$$y_{IF}(t) = x_{IF}(t) + Z(t) \tag{12}$$

3.2.3 | Signal processing flow

The flow chart for the signal processing chain is shown in Figure 2. Since the 4D TDM MIMO radar simulation incorporates all the processes from signal generation to reflection to reception, more realistic radar data representations are obtained. Each sub-block from Figure 2 is described in this section.

- **Range estimation**

There are 256 samples per chirp. The resultant discrete signal waveform in the frequency domain can be derived in

$$X_{IF}[k] = \sqrt{\sigma} e^{j2\pi f_c \tau} P\left(\frac{2\pi}{N_s} k - \frac{2\pi s \tau}{F_s}\right), 0 \le k < N_s \tag{13}$$

where $F_s = 4.096$ MHz is the sampling rate. Function P indicates the DFT of a square window function with $N_s = 256$ samples. In the frequency domain, the peak value of the P function is taken at zero frequency. The frequency of the IF signal is directly proportional to the range of the target as the time of flight of the wave introduces a time shift τ between the transmitted frequency slope and the received frequency slope. The range is derived from the index corresponding to the peak value of $x_{IF}[k]$. Due to the strong sidelobe effect caused by P, the trajectories of some specific body parts with small RCS can be obscured by a stronger target in a neighbouring range bin. To address this problem, the Hanning window function is used to help eliminate sidelobes at the cost of enlarging the main lobe by 100%. We cut out the first 3 s of jumping Jack, kick and walk as time duration to obtain range-time output, while about 2.5 s segment is taken from punch motion since the length of collected data is less than 3 s, which is presented in Figure 4.

- **Velocity estimation**

FMCW radar measures the phase difference between the adjacent chirps to evaluate the velocity of targets, which could
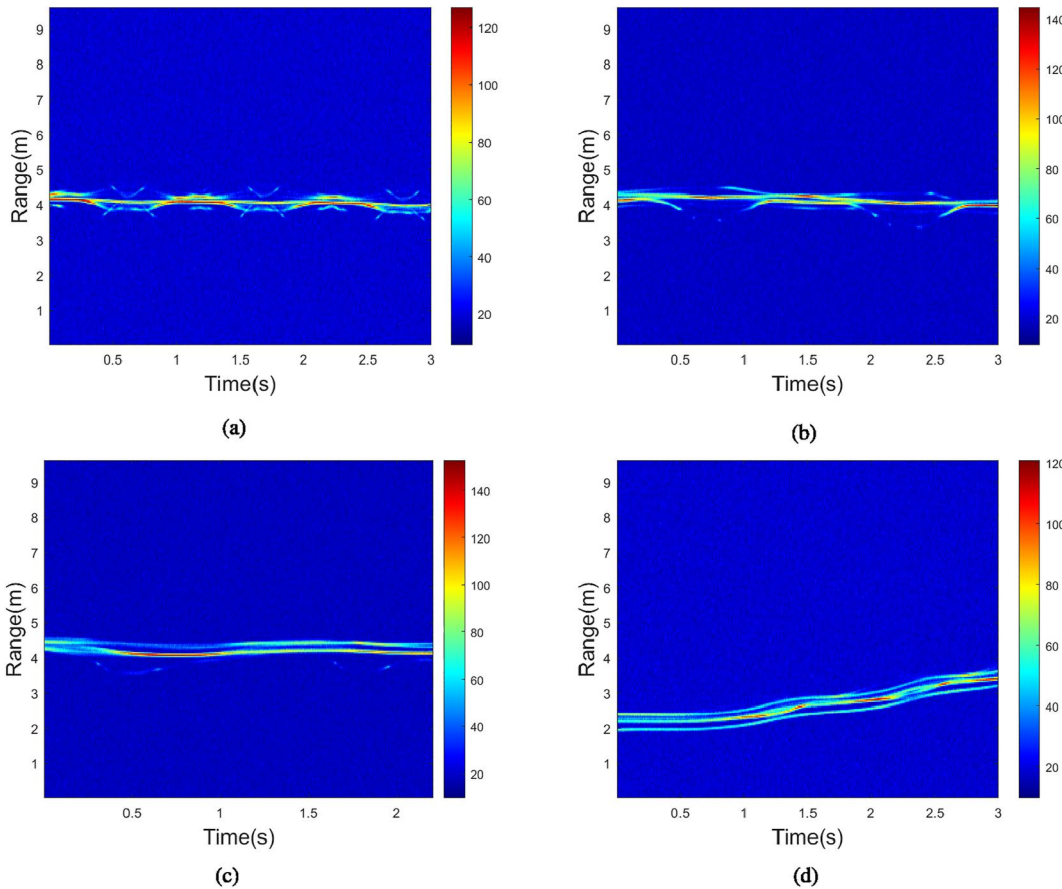

FIGURE 4 Range-time representation of four activities. (a) Jumping Jack. (b) Kick. (c) Punch. (d) Walk.

be reflected in the spectral peak of the secondary FFT across the slow-time dimension. Suppose the target moves at a velocity of v for a whole chirp, then for the kth sample of two adjacent chirps, the phase change can be derived in Equation (14):

$$\Delta\phi = \frac{4\pi v t_c (T_y + T_z)}{\lambda} \quad (14)$$

Then, after the range-DFT across the mth chirp, the IF signal becomes:

$$x_k[m] = X_0[k]e^{jm\frac{4\pi v t_c(T_y+T_z)}{\lambda}} \quad (15)$$

where $X_0[k]$ is the value of the kth sample of DFT across the first chirp, and v refers to the velocity to be estimated. Similar to the method for range DFT, a second DFT for the whole radar frame is performed to extract Doppler information. The Fourier transform of Equation (15) could be presented in Equation (16), where l indicates the index of chirps.

$$X_k[l] = X_0[k]P\left(\frac{2\pi}{N_c}l - \frac{4\pi v t_c(T_y+T_z)}{\lambda}\right), 0 \le l < N_c \quad (16)$$

Since the maximum value of the *sinc* function is taken at the origin, the maximum velocity component can be measured by the peak of $X_k[l]$. However, given that the movement of the human body is complicated and non-rigid, Doppler velocity may be smeared in RDM. In this step, the Hanning window function is applied as well. After DFTs on fast-time and slow-time dimensions are implemented independently on each channel, we generate the range-Doppler map (RDM) as the 2D CFAR process input. Since 2D CFAR is achieved based on the disparity in intensity between noises and effective echoes, the combined RDM is obtained by the incoherent superposition of all considered virtual channels. Figure 5 illustrates the representative RDM of four activities during one radar frame.

- **2D CFAR**

The objective of the 2D CFAR algorithm is to distinguish noise and clutter from the target signal according to the decision threshold of individual test units in RDM [23, 24]. As little prior knowledge about the average noise level in a radar receiver is obtained, it must be evaluated in the first step of the decision process. A reference window is used to detect the target compared to the average noise level in the local RDM. The Cell Under Test is surrounded by a guard band of 2 cells and a training band of 4.
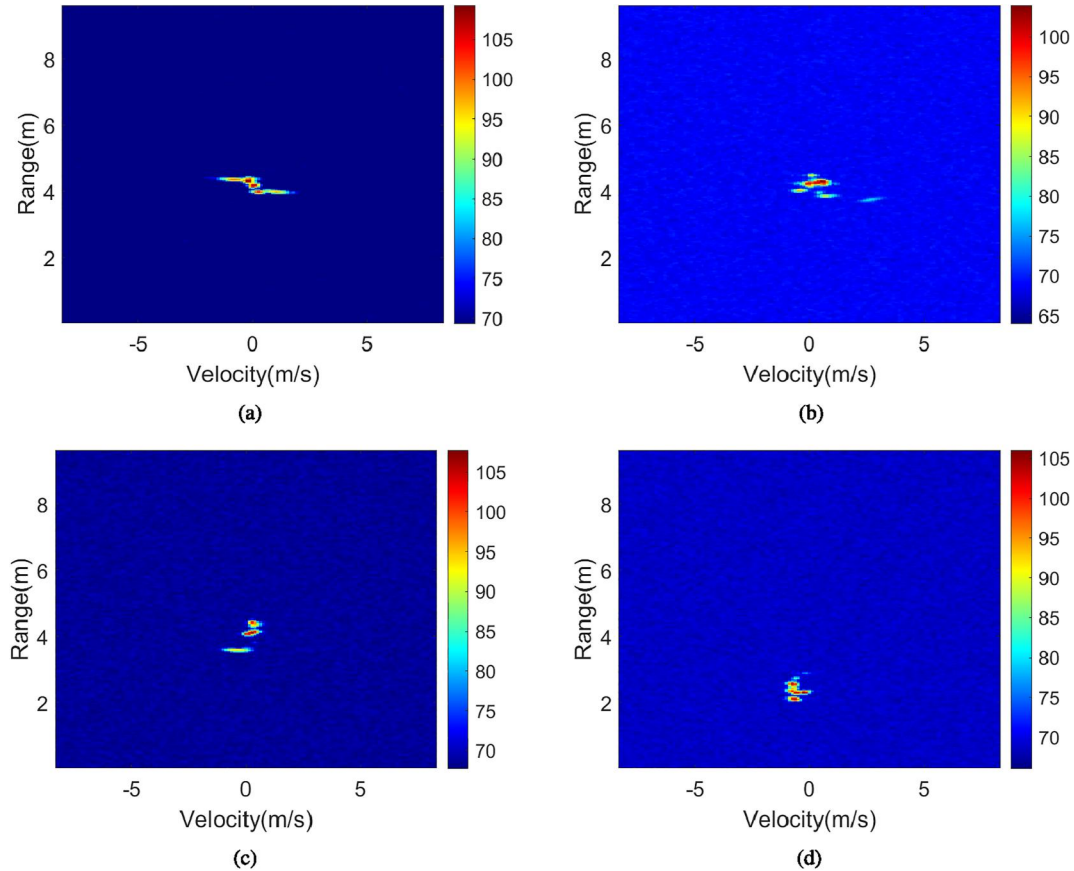

FIGURE 5 Range Doppler map of four activities. (a) Jumping Jack. (b) Kick. (c) Punch. (d) Walk.

In this part, 2D Cell Averaging CFAR (CA-CFAR) and Order Statistics CFAR (OS-CFAR) algorithms are applied on a single channel and MIMO channels to compare the performance of target detection. In Figure 5a for example, we plot the 2D CFAR results of the jumping Jack on the RDM surface in Figures 6 and 7.

In Figure 6a,b, 2D CFAR processing is performed on the first virtual channel, while in Figure 7a,b, it is conducted on the combined RDM. We assume the intensity thresholds of RDM for a single channel and combined channels are 50 and 85 dB, respectively, which means that RDM parts with higher intensity than the threshold will be considered real targets. To compare the performance of different CFAR schemes, precision and the missing rate are introduced. Precision is defined as the proportion of the number of correctly detected targets to that of all detected dots, while the missing rate is defined as the proportion of the number of missing targets to that of all real targets. Both of these parameters are calculated and presented in Table 3. The use of MIMO OS-CFAR compared to one-channel OS-CFAR reduces the number of wrongly detected targets considerably by 6.66% and increases the detection rate by 37.34%.

From Table 3, it is clear to figure out that 2D CFAR methods conducted on the combined RDM result in higher precision and less target-missing rate than that of SISO systems. Although the precision of MIMO-CA CFAR is 100%, it misses most targets in the RDM. In contrast, only around 5% of targets are not detected by the MIMO OS-CFAR process. Therefore, MIMO-OS CFAR almost retains complete information about actual targets. MIMO OS-CFAR can therefore automatically identify the regions of interest, which are ideal for our HAR application compared to the other 3 methods in this paper. Other CFAR methods may perform better and new
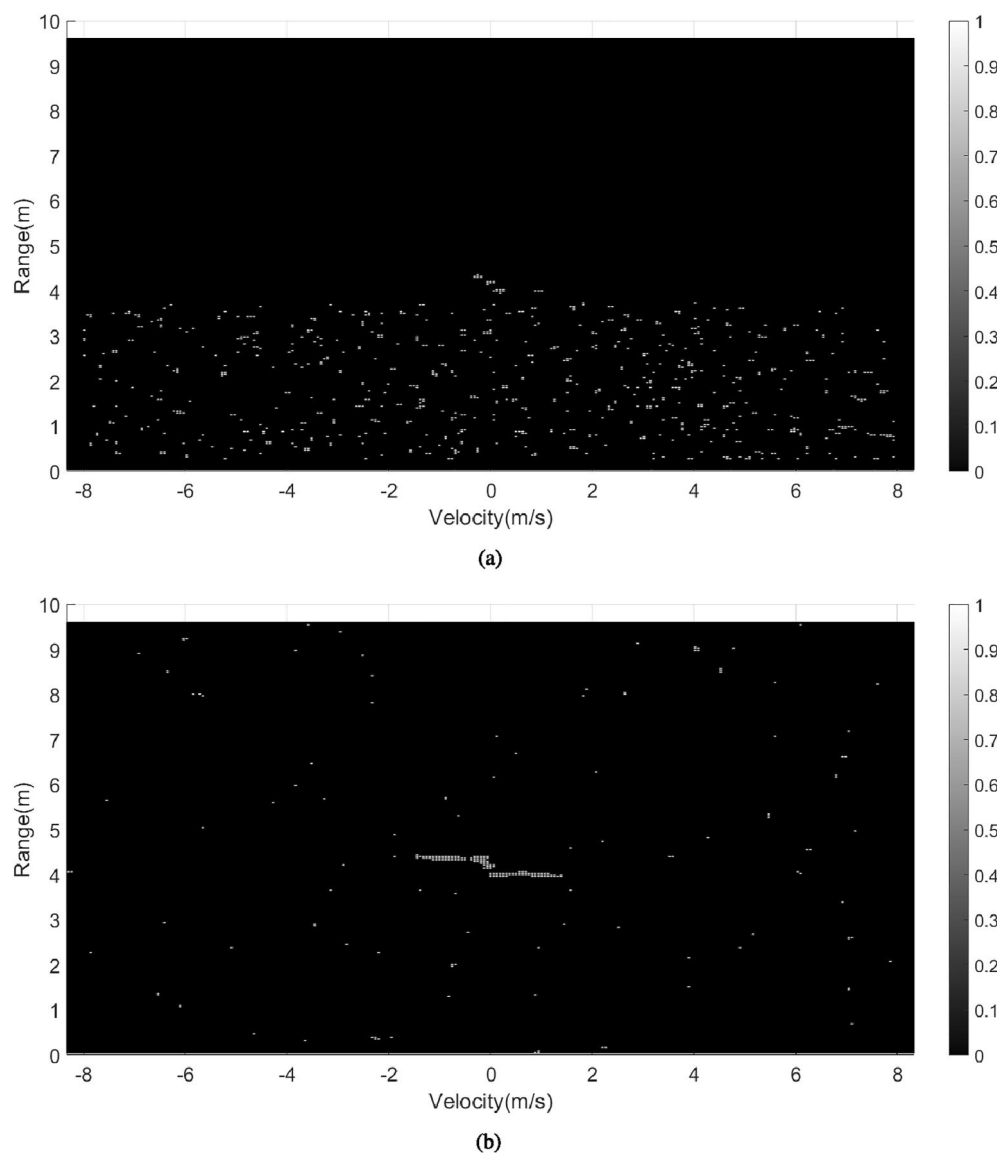
FIGURE 6 2D constant false alarm rate (CFAR) detections on the range Doppler map surfaces on the first virtual channel for the jumping Jack activity. (a) SISO-CA CFAR. (b) SISO-OS CFAR.
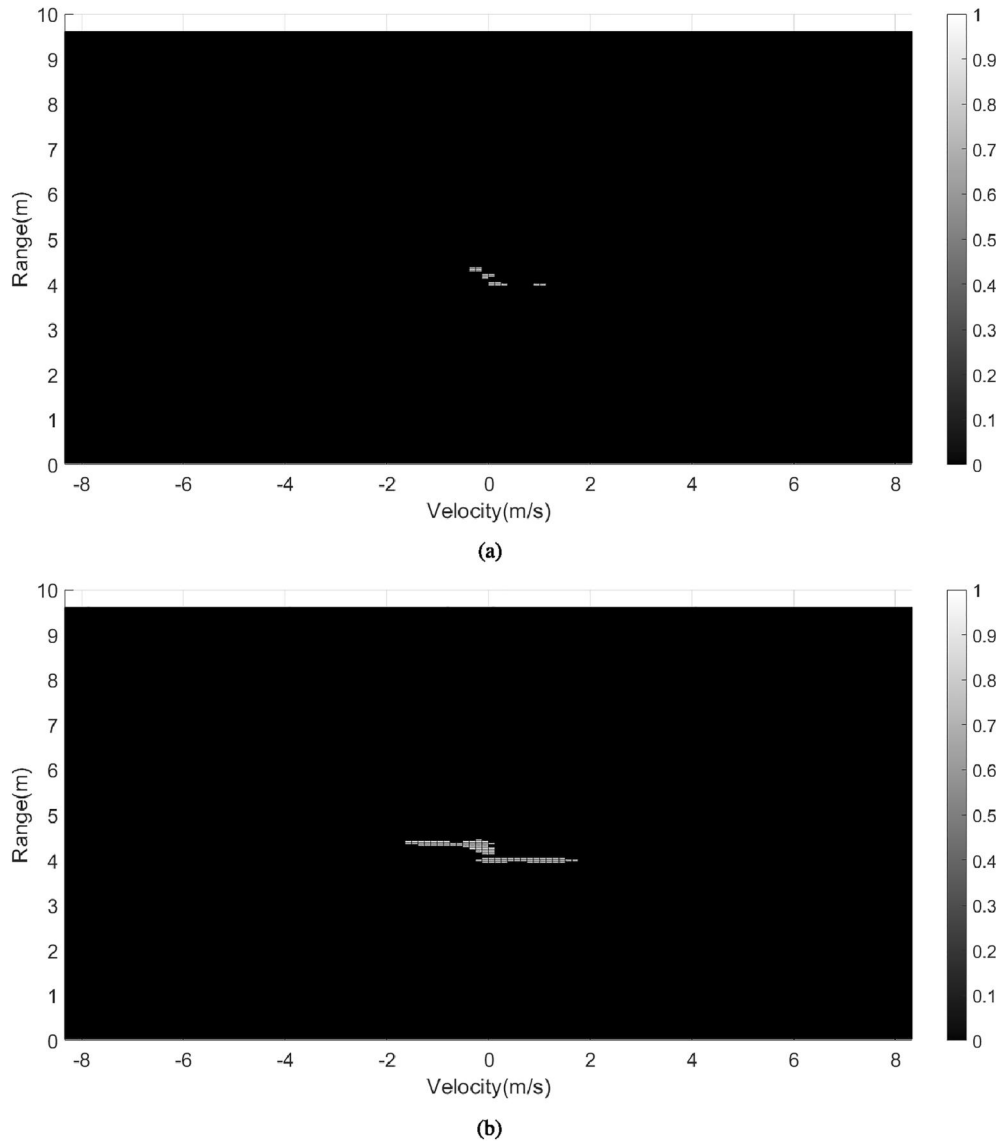
FIGURE 7 2D constant false alarm rate (CFAR) detections on the range Doppler map surfaces combining MIMO channels for the jumping Jack activity. (a) MIMO-CA CFAR. (b) MIMO-OS CFAR.

TABLE 3 Performance comparison of different constant false alarm rate schemes.

2D CFAR scheme	SISO-CA	SISO-OS	MIMO-CA	MIMO-OS
Precision	3.57%	41.85%	100%	79.19%
Missing rate	82.17%	11.72%	75.95%	5.06%

CFAR algorithms are routinely proposed that are application-specific but this is outside the scope of this paper.

• **Micro-Doppler (mD) signatures**

Short-time Fourier transform (STFT) is a widely used tool for analysing mD signatures. It applies the Fourier transform to overlapping signal segments, typically with a window function applied to each segment to reduce spectral leakage. The window function helps taper the signal within each segment to reduce the side effects of abrupt changes at the edges of the segment. By analysing the mD signatures, changes in the frequency content of a signal over time determine the periodicity of activities.

The MATLAB® function 'spectrogram' with a sliding window length of 128 and an overlap factor of 95% are applied on the first channel to perform STFT. The mD signatures of four different activities are shown in Figure 8.

Figure 8 shows that four activities contain different peak amplitude and variation tendencies of Doppler velocity. For instance, the speed of the jumping Jack vibrates more dramatically than another three do, and its peak value is much larger than that of walking. In addition, various activities may
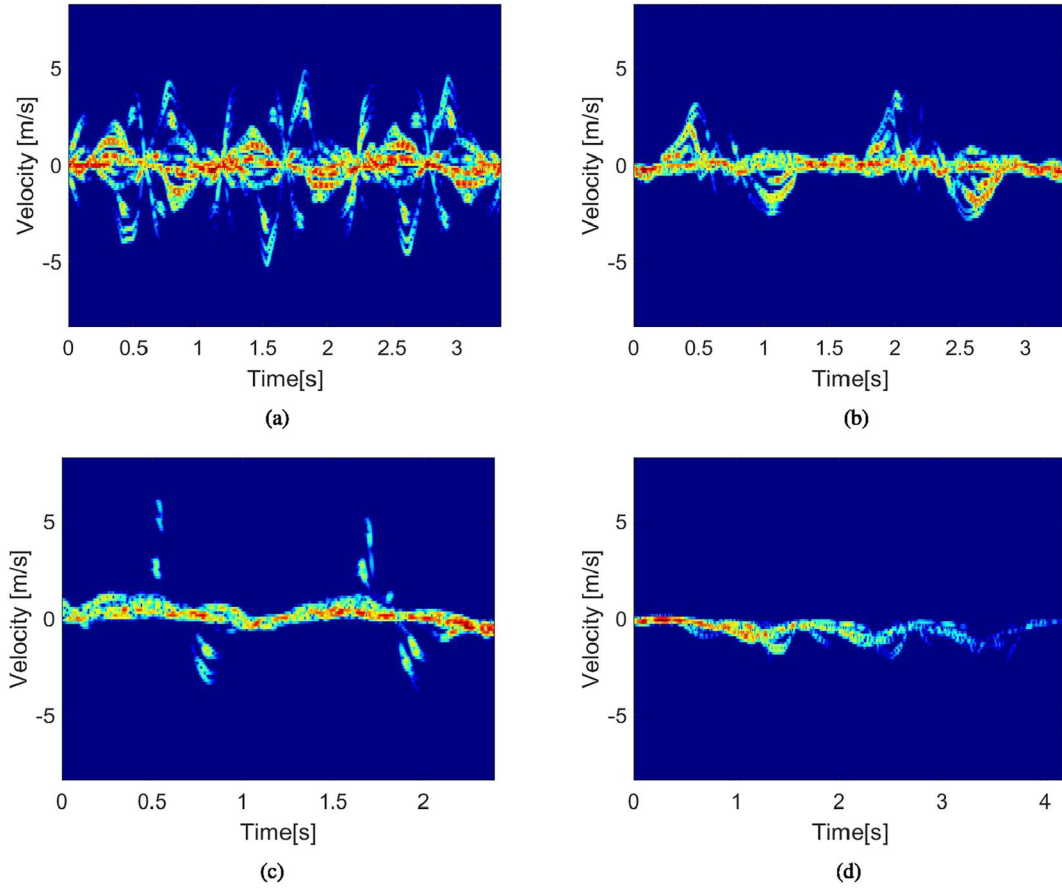
FIGURE 8 Micro-Doppler signature of four activities. (a) Jumping Jack. (b) Kick. (c) Punch. (d) Walk.

have different periods. For jumping and punching, the movement period is about 1 s, while the period is around 1.5 s for kicking and walking. This conclusion is also applied in generating range-Doppler-time (RDT) profiles to determine time duration.

- **Range-angle representation**

The direction of the target is determined by measuring the angle at which the wavefront of the echo reaches the radar. The direction of the incident wavefront can be determined by measuring the phase difference received by separate antennas. Suppose $N_y = T_y \cdot R_y = 48$ is the number of channels along the y axis, and i indicates the virtual channel index. Then, for kth sample at the lth chirp, Doppler-DFT derived from the ith channel is as follows:

$$X_k^i[l] = X_0^0[k]P\left(\frac{2\pi}{N_c}l - \frac{4\pi vt_c(T_y + T_z)}{\lambda}\right)e^{ji\frac{2\pi d_r sin(\alpha)}{\lambda}}, \quad (17)$$

where k and l are selected through the OS-CFAR algorithm from the combined RDM, representing indexes of range and velocity. As the MIMO radar works in the TDM mode, phase compensation is necessary [17]. When the time interval of two

adjacent chirps is t_c, an additional wave path difference is likely to be induced due to the velocity of the target, leading to another phase shift, which should be excluded. After the compensation, we can derive $X_{k,l}[q]$ and extract angle information by applying DFT across virtual channels.

$$X_{k,l}[q] = X_0^0[k]P\left(\frac{2\pi}{N_c}l - \frac{4\pi vt_c(T_y + T_z)}{\lambda}\right)$$
$$P\left(\frac{2\pi}{N_y}q - \frac{2\pi d_r sin(\alpha)}{\lambda}\right), 0 \leq q < N_y \quad (18)$$

The azimuth and elevation could be estimated with the maximum value. Since some body parts are detected as targets after OS-CFAR, their range and speed can be determined. The range-angle representation is obtained by summing radar-angle matrices of all detected targets. Figure 9 shows the range-azimuth and range-elevation profiles of jumping Jack activity during the first radar frame, where the axes X(m), Y(m), and Z (m) refer to the targets' coordinates relative to the radar; D(m) is the distance between the radar and projection of targets to the plane formed by x axis, y axis, and radar.

In Figure 9a,b, the azimuth and elevation of the detected targets are close to 0°. It is desirable because our simulated
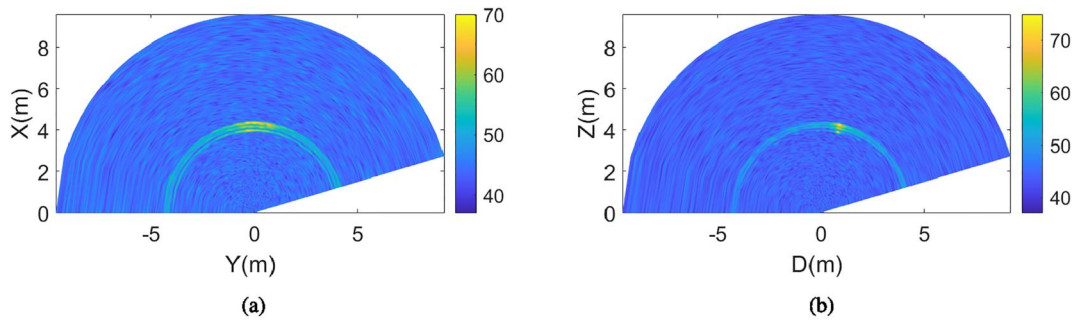
FIGURE 9 Power spectrum for the time-division multiplexing MIMO radar in the range-angle domain. (a) Range-azimuth profile. (b) Range-elevation profile.

radar has a high angular resolution surrounding 0°, which reaches up to 2.38°.

3.2.4 | Point clouds representation

For simulation, two methods of point cloud representation are tested for activity recognition. The first one extracts the shape of a human model by calculating Cartesian coordinates from the range-angle representation. The other method combines the OS-CFAR processed RDM surfaces over a time window to extract an RDT representation. A sampling algorithm is applied to turn the RDT surface into a point cloud.

(I) **Based on spatial position**

To generate point clouds from the range-angle representation from the detected targets, the space coordinates of the target (x_t, y_t, z_t) can be derived as follows:

$$\begin{cases} x_t = r\cos(\beta)\cos(\alpha) + x_R \\ y_t = r\cos(\beta)\sin(\alpha) + y_R \\ z_t = r\sin(\beta) + z_R \end{cases} \quad (19)$$

Each point cloud image is produced from each radar frame, and all images obtained during one period of the activity form a time-series sequence, which allows us to use a neural network for classification, such as Point-Net + Long Short Term Memory [25]. Point cloud images of four activities generated from the first radar frame are illustrated in Figure 10.

(II) **Based on range-Doppler time (RDT)**

The RDS is constructed after the 2D OS-CFAR on the RDM representation that helps distinguish targets from clutter and noise. Compared with the construction method proposed in [9], the whole parts detected by CFAR are retained instead of the contour of separate body parts. For those detected targets, their intensity is set to 1, while other cells are valued as 0, shown in Figures 6 and 7. As discussed before, the time to complete the activities of jumping Jack and punching is about 1 s and about 1.5 s for kicking and walking. Therefore, we can

plot all filtered RDM slices in a 3D volume within one period and extract an iso-value surface. To compensate for lost information in the individual frame and the absence of correlation between consecutive frames, the sliding window (0.1 s) with an overlap of 0.025 s (25%) is applied to produce more RDM slices. The MATLAB® function 'isosurface' creates a surface with the same intensity value by pre-setting a threshold. The intensity threshold is set to 0.5 as the intensity of our desired targets has been binarised to 0 for no detection and 1 for detected targets. Figure 11 shows the RDT plots of four different activities, which are, respectively, obtained from the files jumpingJack3Reps (001_120.amc), kickLSide2Reps (001_120.amc), punchLSide2Reps (001_120.amc), and walkLeft3Steps (001_120.amc) from the HDM05 database [20].

Range-Doppler surface describes valuable information from the perspective of range, velocity and time, which consists of thousands of vertices. To obtain point clouds, the geometrical centre sampling method is applied. In practice, samples are taken at the centre of all triangles, and 3000 points are re-sampled randomly. Figure 12 shows the cloud points of four activities generated from one period of each after RDS sampling.

3.3 | Classification model

3.3.1 | Data preparation

Before the point clouds of four activities are created, we conduct an overall feasibility analysis of the two schemes of point cloud representation mentioned above.

4D radar provides elevation information, so it can provide more accurate contour information about the target, which is one of the vital input characteristics of target classification. However, during relative movement between radar and target, the position change of the scattering centre and intensity will also perform non-linear modulation of echo amplitude. Hence, the description of the target shape is not stable over time. Furthermore, point clouds based on spatial position only
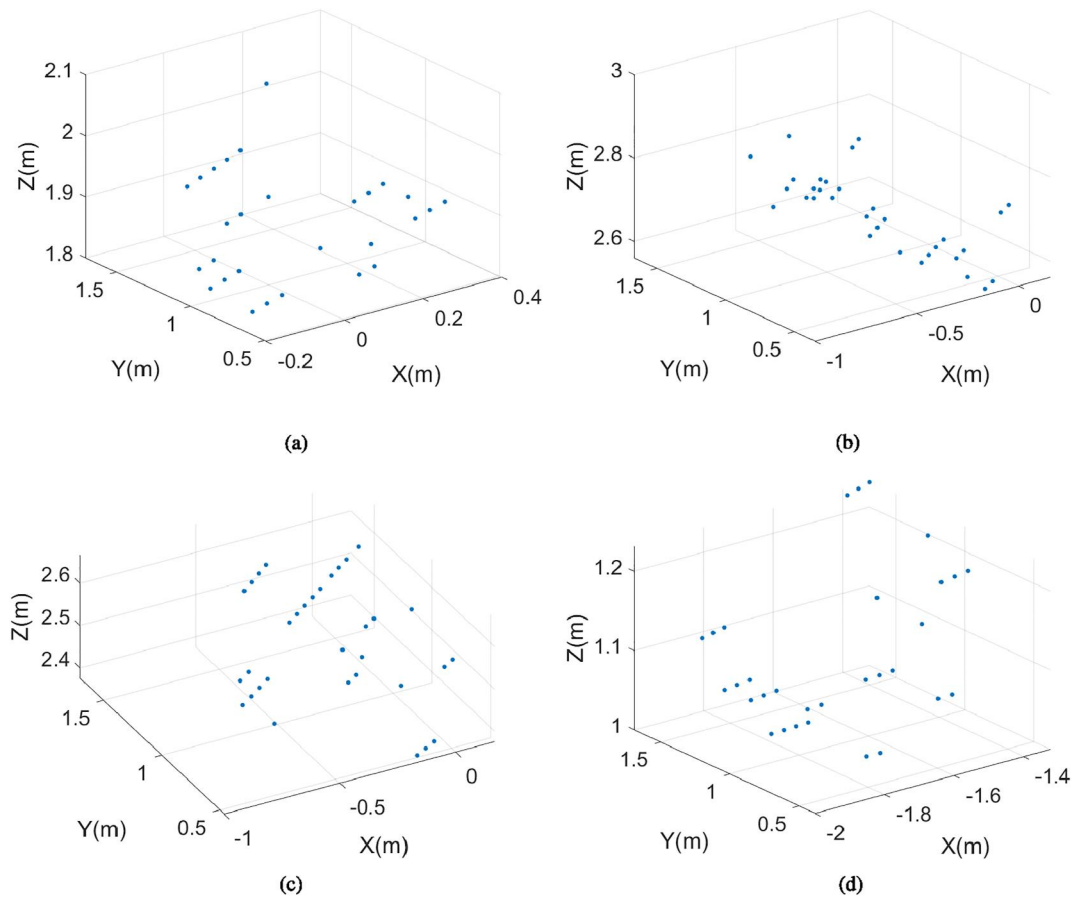
FIGURE 10 Point clouds of four different activities. (a) Jumping Jack. (b) Kick. (c) Punch. (d) Walk.

contain information about x, y, and z coordinates, which ignore Doppler information and produced a very poor performance with less than 50% accuracy, which is not suitable.

In comparison, the method based on RDT combines information around range, velocity and time duration, providing useful features for classification. Therefore, the RDT representation is determined for simulation to produce a point cloud dataset.

100 cloud images for four activities are generated from the mocap dataset, and each graph contains 3000 sampling points. Typically, the data are divided into training sets and test sets. Given the limited number of samples, 10-fold cross-verification is applied. The average value of 10 evaluations is taken as the classification accuracy of the model. Totally, 360 (90%) training samples and 40 (10%) testing samples are produced.

3.3.2 | PointNet

Micro-Doppler simulations can be extrapolated to 4D radar. Adding the other data representation from the perspective of the range domain allows us to extract point clouds, and PointNet is proven as an effective model to process point clouds for classification and segmentation [11, 26]. It was one of the first deep learning approaches that directly operated on

unordered point cloud data without relying on meshing techniques. The main idea is to use shared multi-layer perceptions to extract the global feature and output the classes. This network greatly retains the characteristics of point clouds including the rotation in-variance and permutation in-variance by applying T-net and max-pooling, respectively. PointNet can be divided into a feature-extraction network and a classification network. Before point clouds are sent into the feature-extraction network, point clouds are pre-processed through normalisation, decentralisation and argumentation. In addition, since the generated dataset is small, large quantities of points for each point cloud image may lead to difficulty in training the model. Therefore, each RDT profile is re-sampled to contain 500, 1000, 2000, and 3000 points through random selection as network input. Firstly, we take the number of points as 1000 to train our model and then make a comparison with the other two cases. Since point clouds are unordered, a micro-network (T-Net) is used to obtain a spatial transformation network and adjust point clouds to a uniform pattern for better recognition, which is the input transformation. After passing an MLP, a transformation matrix (feature transformation) and MLP are applied again to create a $n \times 1024$ tensor, where n is the number of points. Then, the global feature is obtained by conducting max pooling to the tensor. For the classification task, an MLP with full connection is employed and then scores
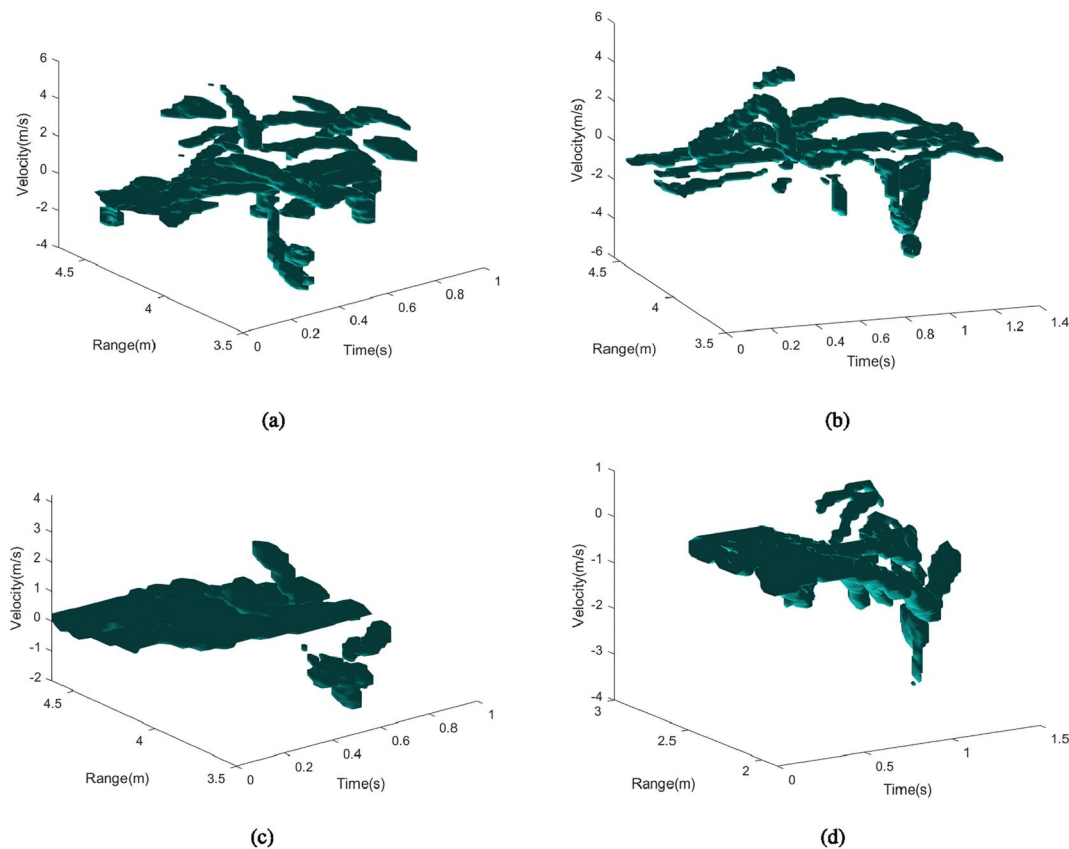
FIGURE 11   Range-Doppler surface of four different activities. (a) Jumping Jack. (b) Kick. (c) Punch. (d) Walk.

for four activities are calculated. During the training, NLLLoss is applied as the loss function [11]. The structure of PointNet is shown in Figure 13.

At the first trial, the batch size is set to 3. The initial learning rate is 10^{-6}, and we apply the Adam optimiser to update the learning rate every 10 samples. In addition, the dataset is shuffled every epoch to avoid the effect of the input sequence on network training. The accuracy and loss curves are presented in Figure 14.

From Figure 14, the training accuracy keeps a low level and much less than that of testing. The training accuracy fluctuates around 30%, and the testing accuracy is less than 60%. Furthermore, it is hard for training loss and testing loss to drop down, which may result from the small learning rate. To optimise it, we changed the learning rate to 10^{-4} and plot the loss and accuracy curves shown in Figure 15.

Figure 15 shows 200 epochs of the training process. The training model has converged since the loss has levelled off at ˜0.65. In addition, the testing accuracy is ˜10% higher than the training accuracy. One possible reason for this phenomenon is the small sample size. If the distribution of the training set and the test set is not uniform, and the model can correctly capture the distribution pattern within the data, the internal variance of the training set may be more significant than that of the verification set, resulting in error judgement of the training set.

We saved the model parameters of the 160th epoch as the final result, which achieves 87.2% testing accuracy. For another nine iterations, the initial learning rate is fixed to 10^{-4} for training. The step size and rate of attenuation are 10 and 0.5, respectively, which indicate that the learning rate is reduced by half every 10 batches.

4 | RESULTS AND DISCUSSION

Similar to the previous discussion, the number of points for each cloud image is re-sampled to 500, 2000 and 3000. Then models are trained for 10 iterations, respectively, the results of which are listed in Table 4.

From the tables shown above, we find that the average value of testing accuracy using 1000 samples in one point cloud is the highest, reaching 90.0%. The median value of all testing accuracy is 92.3%, and the 25th and 75th percentiles are 87.2% and 92.3%, respectively. This interval shows the robustness of our model. The lowest accuracy is 79.5% and the maximum is 94.9%. The confusion matrix in Figure 16 is shown for the highest accuracy (94.9%).

The graph shows that only 39 samples are tested, which is one less than our testing set. This is because the batch size is set to 3, and the last sample is dropped to guarantee that the
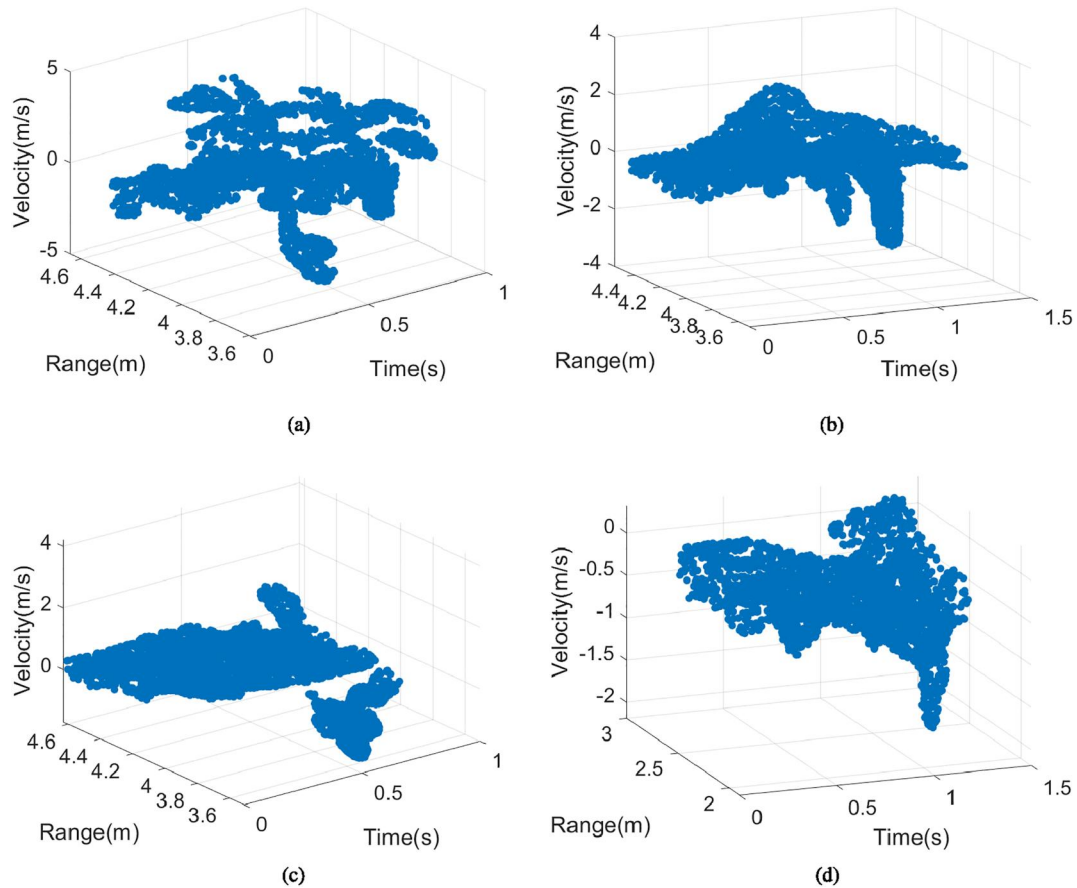
FIGURE 12 Point clouds using range-Doppler time (RDT) representation. (a) Jumping Jack. (b) Kick. (c) Punch. (d) Walk.
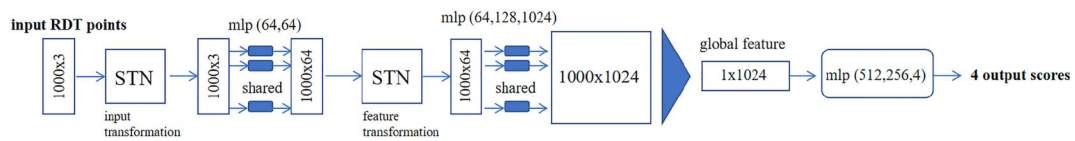

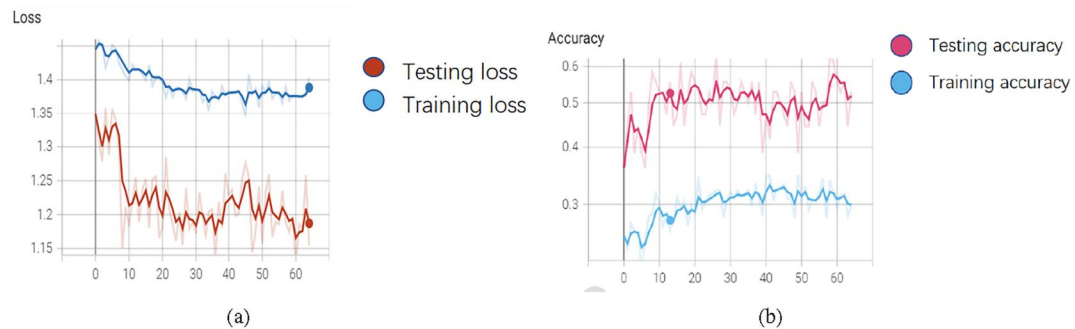**FIGURE 13** The structure of PointNet.

FIGURE 14 Loss curve and accuracy curve when the learning rate is 10^{-6}—The shaded curves represent the raw data and the trend lines are calculated using an exponential moving average. (a) Loss-epoch. (b) Accuracy-epoch.

number of testing samples is an integer of multiple of the batch size. Consequently, there are 11 testing samples for jumping Jack, 9 samples for kick, 11 samples for punch, and 8 samples for walk. Furthermore, the wrong prediction occurs between the kick and punch, and individual testing accuracy for the jumping Jack, kick, punch and walk are 100%, 77.8%, 100%, and 100%, respectively. Therefore, only the kick activity is causing problems in classification.

FIGURE 15 Loss curve and accuracy curve when the learning rate is 10^{-4}. The shaded curves represent the raw data and the trend lines are calculated using an exponential moving average. (a) Loss epoch. (b) Accuracy epoch.

TABLE 4 Relation between the number of sampled points and testing accuracy.

Number\Accuracy\Iteration	1	2	3	4	5	6	7	8	9	10	Average value
500	94.9%	87.2%	92.3%	69.2%	87.2%	84.6%	84.6%	92.3%	87.2%	76.9%	85.6%
1000	87.2%	94.9%	92.3%	92.3%	79.5%	92.3%	94.9%	87.2%	92.3%	87.2%	90.0%
2000	94.9%	89.7%	92.3%	76.9%	94.9%	87.2%	87.2%	94.9%	87.2%	82.1%	88.7%
3000	82.1%	79.5%	87.2%	74.4%	71.8%	71.8%	84.6%	84.6%	87.2%	74.4%	79.8%
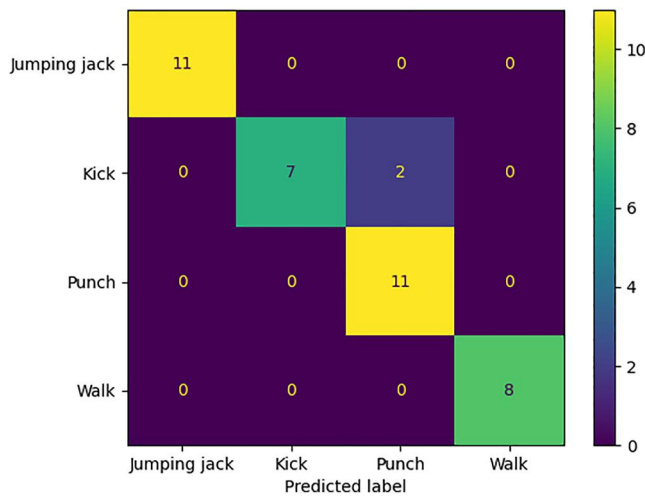
FIGURE 16 Confusion matrix of four activities.

5 | CONCLUSION AND FURTHER WORK

5.1 | Conclusions

In the paper, we build a 4D TDM radar model with 12 Tx and 16 Rx antennas that can simulate the MIMO radar signal processing. Profiles of range-time, spectrogram, range-Doppler and range-angle are obtained, and it is verified that MIMO 2D OS-CFAR performs better than CA-CFAR. HDM05 mocap dataset is utilised to produce a human skeleton model, and activities including jumping Jack, kick, punch and walk are selected to create point clouds through the RDT algorithm. PointNet is chosen as the classification network for point clouds and average classification accuracy reaches 90%.

5.2 | Suggestions for further work

Regarding the time consumption, it takes about 1.5 h to generate one point cloud image using RDT representation using the platform 12th Gen Intel(R) i9-12,900H. Some steps are highly time-consuming like IF signal generation for each channel, OS-CFAR filter and iso-surface extraction. Therefore, more time-efficient programming is expected and parallelisation of the code would improve efficiency as the Rx channels are processing the Rx signals separately before being joined for the RDM, range-angle and micro-Doppler representations. We are currently developing a bespoke 4Tx-4Rx MIMO radar platform at the University of Glasgow that we will combine with our Mocap to verify the accuracy of this simulator once the radar will be operational. Regarding activity recognition, only 400 point cloud images of four activities are generated for training, which is quite limited and may lead to the underfitting of the model. The University of Glasgow has its own motion capture suite and we will collect a more extensive database of representative activities for assisted living. The human model is still quite simplistic and we will work with the Unreal Engine 5 to generate avatars to have more realistic human models and reflective surfaces to better simulate radar data representations.

AUTHOR CONTRIBUTIONS

Junyu Zhou: Formal analysis; investigation; software; validation; writing—original draft. **Julien Le Kernec**: Conceptualization; methodology; project administration; supervision; writing—review and editing.

CONFLICT OF INTEREST STATEMENT
None.

DATA AVAILABILITY STATEMENT
The code for the simulator is available at https://github.com/JASONZ777/4D-radar-simulator.git.

ORCID
Julien Le Kernec https://orcid.org/0000-0003-2124-6803

REFERENCES
1. Mobiquity: Interactive Digital Healthcare Features Radar, Mobiquity Hexware (no date). https://www.mobiquity.com/insights/interactive-digital-healthcare-features-radar. Accessed 21 April 2023
2. Wolff, D.-I.F.H.C.: Radar Basics, Radartutorial (no date). https://www.radartutorial.eu/01.basics/!rb02.en.html. Accessed 21 April 2023
3. Chen, V.C.: The Micro-doppler Effect in Radar. Artech House, Norwood (2019)
4. Ochieng, F.X., et al.: Deflection characterisation of rotary systems using ground-based radar. J. Eng. 2019(20), 7215–7219 (2019). https://doi.org/10.1049/joe.2019.0503
5. Zhou, B., et al.: Simulation framework for activity recognition and benchmarking in different radar geometries. IET Radar, Sonar Navig. 15(4), 390–401 (2021). https://doi.org/10.1049/rsn2.12049
6. Tang, C., et al.: Augmenting experimental data with simulations to improve activity classification in healthcare monitoring. In: 2021 IEEE Radar Conference (RadarConf21), pp. 1–6. Atlanta (2021). https://doi.org/10.1109/RadarConf2147009.2021.9455314
7. Li, X., et al.: Hierarchical radar data analysis for activity and personnel recognition. Rem. Sens. 12(14), 2237 (2020). Available at:. https://doi.org/10.3390/rs12142237
8. He, Y., et al.: Range-Doppler surface: a tool to analyse human target in ultra-wideband radar," IET Radar. Sonar & Navigation 9(9), 1240–1250 (2015). Available at: doi:. https://doi.org/10.1049/iet-rsn.2015.0065
9. Li, M., Chen, T., Du, H.: Human behavior recognition using range-velocity-time points. IEEE Access 8, 37914–37925 (2020). Available at:. https://doi.org/10.1109/access.2020.2975676
10. Sengupta, A., et al.: Mm-pose: real-time human skeletal posture estimation using mmWave radars and CNNs. IEEE Sensors Journal, 20, (17), 10044 (2020). https://doi.org/10.1109/jsen.2020.2991741
11. Charles, R.Q. et al.: PointNet: deep Learning on point sets for 3D classification and segmentation. In: 2017 IEEE Conference on Computer Vision and Pattern Recognition (CVPR) (2017). https://doi.org/10.1109/cvpr.2017.16
12. Gong, P., Wang, C., Zhang, L.: MMPoint-GNN: graph neural network with dynamic edges for human activity recognition through a millimeter-wave radar. (2021).2021 International Joint Conference on Neural Networks (IJCNN) [Preprint]. https://doi.org/10.1109/ijcnn52387.2021.9533989
13. Singh, A.D. et al.: Radhar. In: Proceedings of the 3rd ACM Workshop on Millimeter-Wave Networks and Sensing Systems [Preprint] (2019). https://doi.org/10.1145/3349624.3356768
14. Chen, S.C.-Y.: Signal Processing Algorithms for MIMO Radar (2009)
15. Johnston, J., et al.: MIMO OFDM dual-function radar-communication under error rate and beampattern constraints. In: IEEE Journal on Selected Areas in Communications, vol. 40, pp. 1951–1964 (2022). https://doi.org/10.1109/JSAC.2022.3156651
16. Wei, Z., et al.: Orthogonal time-frequency space modulation: a promising next-generation waveform. In: IEEE Wireless Communications, vol. 28, pp. 136–144 (2021). https://doi.org/10.1109/MWC.001.2000408
17. Li, X., et al.: Signal Processing for TDM MIMO FMCW millimeter-wave radar sensors. IEEE Access 9, 167959–167971 (2021). Available at:. https://doi.org/10.1109/access.2021.3137387
18. Ender, J.H.G., Klare, J.: System architectures and algorithms for radar imaging by MIMO-SAR. In: 2009 IEEE Radar Conference, pp. 1–6. Pasadena (2009). https://doi.org/10.1109/RADAR.2009.4976997
19. MIMO radar (rev. A) - texas instruments. https://www.ti.com/lit/pdf/swra554 (no date). Accessed 20 April 2023
20. Müller, M., et al.: Documentation Mocap Database HDM05. Technical Report. Universität Bonn (2007). No. CG-2007-2, ISSN 1610-8892
21. de Aguiar, E., Theobalt, C., Seidel, H.-P.: Automatic learning of articulated skeletons from 3D marker trajectories. In: Proc. Intl. Symposium on Visual Computing (ISVC 2006), to Appear (2006)
22. Mahafza, B.R.: Radar Systems Analysis and Design Using MATLAB. Chapman and Hall/CRC (2000)
23. Rohling, H.: Radar CFAR Thresholding in clutter and multiple target situations. In: IEEE Transactions on Aerospace and Electronic Systems, AES-19, pp. 608–621 (1983). https://doi.org/10.1109/taes.1983.309350
24. Li, D., Yu, G.: 2D-os-CFAR detector for cloud clutter suppression. In: 2001 CIE International Conference on Radar Proceedings (Cat No.01TH8559) [Preprint]. https://doi.org/10.1109/icr.2001.984694
25. Kern, N., Grebner, T., Waldschmidt, C.: Pointnet+LSTM for Target list-based gesture recognition with incoherent radar networks. In: IEEE Transactions on Aerospace and Electronic Systems, vol. 58, pp. 5675–5686 (2022). https://doi.org/10.1109/taes.2022.3179248
26. Guo, J., et al.: Complex field-based fusion network for human activities classification with radar. In: IET International Radar Conference (IET IRC 2020), Online Conference, pp. 68–73 (2020). https://doi.org/10.1049/icp.2021.0572

How to cite this article: Zhou, J., Le Kernec, J.: 4D radar simulator for human activity recognition. IET Radar Sonar Navig. 18(2), 239–255 (2024). https://doi.org/10.1049/rsn2.12468